Codoping Effect of Nitrogen (N) to Iron (Fe) Doped Zirconium Titanate ($ZrTiO_4$) Composite toward Its Visible Light Responsiveness as Photocatalysts

Rizka Hayati[1], Rian Kurniawan[2], Niko Prasetyo[1], Sri Sudiono[1], and Akhmad Syoufian[1*]

[1]*Department of Chemistry, Faculty of Mathematics and Natural Sciences, Universitas Gadjah Mada, Sekip Utara, Yogyakarta 55281, Indonesia*

[2]*Institute of Chemical Technology, Universität Leipzig, Linnéstr. 3, 04103 Leipzig, Germany*

* ***Corresponding author:***

email: akhmadsyoufian@ugm.ac.id

Received: November 1, 2021
Accepted: February 19, 2022

DOI: 10.22146/ijc.70146

Abstract: *Iron (Fe) and nitrogen (N) were introduced as dopants into zirconium titanate ($ZrTiO_4$) in order to study the codoping effects of nitrogen on iron-doped zirconium titanate (Fe,N-codoped $ZrTiO_4$) composite. Titanium tetraisopropoxide (TTIP), zirconia (ZrO_2), urea, and iron(II) sulfate heptahydrate were used as the source of TiO_2, semiconductor supports, source of nitrogen, and iron, respectively. A specific amount of iron (1, 3, 5, 7, and 9 wt.%) and a fixed nitrogen content (10 wt.%) were doped into the $ZrTiO_4$ lattice. Various calcination temperatures (from 500 to 900 °C) were also applied to investigate the crystal structure of the composite. The composites were characterized by X-ray powder diffractometer (XRD), Fourier-transform infrared spectrophotometer (FT-IR), scanning electron microscope with energy dispersive X-Ray spectrometer (SEM-EDX), and specular reflectance UV-Vis (SR-UV). The lowest bandgap energy of 2.62 eV was obtained in the composite with 3 wt.% of Fe and 10 wt.% of N calcined at 500 °C.*

Keywords: *codoping; Fe,N-codoped $ZrTiO_4$; composite; iron; nitrogen*

■ INTRODUCTION

Titanium dioxide (TiO_2) has been extensively studied as a semiconductor photocatalyst, attributed to its eminent photocatalytic activity, high chemical stability, high redox ability, photo-corrosion resistance, non-toxicity, and low-price [1-3]. Three major polymorphs of TiO_2 exist in nature, namely anatase, rutile, and brookite [4]. Although the bandgap of anatase (3.2 eV) is slightly higher than rutile (3.0 eV), it exhibits superior photoactivity under UV light irradiation to that of rutile [5]. However, the bandgap of TiO_2 is too large to permit electron excitation under solar light that comprises only about 5% UV energy [6]. Therefore, many efforts have been made to enhance the photocatalytic activity of TiO_2 under the remaining spectrum of solar light, the visible light irradiation.

Modification of TiO_2 can be done by transition metal doping. The interaction of the 3d orbitals of the metal dopant with Ti causes distortion of the surrounding structure and affects the conduction band of the semiconductor [7]. It creates an energy level of impurity within the electronic structure that activates TiO_2 at a low energy wavelength (visible light) [8]. Fe^{3+} species has been considered a favorable candidate among other metal ions due to its similar ionic radii (0.64 Å) to Ti^{4+} (0.68 Å). Thus, Fe^{3+} ions can be easily incorporated into the TiO_2 crystal lattice and decrease the bandgap width, making them more efficient for visible light absorption [9]. Zhang et al. [10] reported in their study that the addition of Fe^{3+} ions to the TiO_2 matrix acts as an electron-hole trap and reduces the recombination rate of the pairs, resulting in the extension of the light absorption band. Nevertheless, there are some drawbacks of using metal dopants, i.e. photo-corrosion and thermal instability. Hence, deep-level defects may form as recombination centers, lowering photocatalytic efficiency [11-12].

The addition of non-metal as codopant has received much interest due to its synergistic impact on improving the visible light absorption [13]. Nitrogen is the most suitable and frequently used as a non-metal doping

element [14]. Nitrogen as a non-metal dopant has many advantages, including chemical stability, low ionization energy, and the atomic size similarity to oxygen. Incorporation of N dopant into the TiO_2 lattice can occur at substitutional or interstitial positions, affecting electron density and charge distribution, thus leading to increased photocatalytic ability [1]. Sinhmar et al. [15] prepared Ni and N codoped TiO_2 catalyst by surface impregnation method and revealed a high performance for photodegradation of phenol under visible light irradiation. It was reported that 2p states of N mixed with O 2p states lead to bandgap narrowing [16]. Di Valentin et al. [17] confirmed that N 2p states occupy slightly above the O 2p valence band, causing a redshift in the valence band edge.

Zirconia (ZrO_2) is another semiconductor with several advantages: predominant thermal properties, high refractive index, high optical transparency, and polymorphic nature [18-19]. Hybrid material of TiO_2 with ZrO_2 is investigated and expected to improve the thermal stability of TiO_2. Syoufian et al. [20] successfully combined ZrO_2 and TiO_2 using sulfonated polystyrene as a template, resulting a hollow spheres material called zirconium titanate ($ZrTiO_4$). According to Kim et al. [21], the coupling of ZrO_2/TiO_2 enhances the photocatalytic activity, owing to its relatively large surface area, small crystalline size, and well-crystallized anatase phase. Incorporating Zr^{4+} into TiO_2 can create lattice defects that allow higher photoactivity than pure oxides. The defects prevent charge recombination by acting as charge-trapping sites [22].

Several methods have been reported for preparing undoped and doped TiO_2 composites, including hydrothermal, sol-gel, microwave, and impregnation [10,23-25]. The utilization of lower reaction temperatures is a typical aspect of these approaches. The reaction processes conducted in the gas or liquid phase allow substantially quicker diffusion than typical solid-state techniques. Among those, the sol-gel process is the most commonly used method because of its many advantages such as simplicity, precise composition control, inexpensive, and ability to produce high purity products [26-27]. The sol-gel method mixes components homogeneously at the molecular level, which is convenient for the dopant incorporation process in the material matrix [28]. Ning et al. [29] observed the presence of Ti–O–Zr links in $ZrTiO_4$ gel produced using the sol-gel process, which possesses a higher oxygen vacancy concentration that enhances photocatalytic activity.

Table 1. Bandgap value of M-$ZrTiO_4$ at the optimum condition (M = Fe, Cu, Zn, and Co)

Material	Eg (eV)
7% Fe-$ZrTiO_4$ 500 °C	2.83 [30]
5% Cu-$ZrTiO_4$ 500 °C	2.87 [31]
5% Zn-$ZrTiO_4$ 900 °C	2.87 [32]
3% Co-$ZrTiO_4$ 500 °C	2.94 [33]

Previous studies of doping on $ZrTiO_4$ composite materials with transition metals Fe, Cu, Zn, and Co have been done. The optimum conditions for the dopant content and calcination temperature obtained for each transition metal are shown in Table 1. Zirconium titanate with 7 wt.% of Fe and calcination temperature of 500 °C has the lowest bandgap value of 2.83 eV. In this work, iron and nitrogen codoped zirconium titanate composite (Fe,N-codoped $ZrTiO_4$) was prepared by the sol-gel method. It has the potential to provide a synergistic effect by expanding the light absorption edge and increasing the efficiency of photocatalysis. Titania was grown on the surface of zirconia to form a material with higher thermal stability compared to pure TiO_2. Both metal and non-metal dopants, i.e., Fe and N, were incorporated into the $ZrTiO_4$ system in order to shift the absorption ability of the material to the visible range. Various dopant contents and calcination temperatures were applied to observe the absorption shift and crystal structures.

■ EXPERIMENTAL SECTION

Materials

Titanium(IV) tetraisopropoxide (TTIP) (97%, Sigma-Aldrich) and ZrO_2 fine powder (Jiaozuo Huasu) were used as the precursor of TiO_2 and supporting semiconductor, respectively. Iron(II) sulfate heptahydrate ($FeSO_4{\cdot}7H_2O$) (Merck) and urea (PA, Merck) were chosen as the dopant sources. Absolute ethanol (PA, Merck) and demineralized water (Jaya Sentosa) were used as solvents.

Instrumentation

X-ray powder diffractometer (XRD) PANalytical X'Pert PRO MRD (Cu Kα radiation λ = 1.54 Å, 40 kV, 30 mA) was used to examine the crystalline structure of the materials. Fourier transform infrared spectrophotometer (FTIR, Thermo Nicolet Is10) was utilized to observe vibrational spectra of functional groups in the materials. The morphology and elemental composition of materials were analyzed using a scanning electron microscope with an energy dispersive X-Ray spectrometer (SEM-EDX). The bandgap was determined from the absorption spectra, obtained using specular reflectance UV-Vis spectrometer UV 1700 Pharmaspec (SR-UV).

Procedure

Fe,N-codoped $ZrTiO_4$ was synthesized by the sol-gel method. All sol-gel processes were performed at room temperature. First, 2.5 mL of TTIP as Ti precursor was dissolved in 25 mL of absolute ethanol and stirred for 10 min at 700 rpm, resulting in a colorless and transparent Ti solution. Meanwhile, 1 g of ZrO_2 powder, 86.61 mg of urea (10 wt.%), and $FeSO_4{\cdot}7H_2O$ with different loadings (20.11, 60.34, 100.55, 140.78 and 181.01 mg) for 0, 1, 3, 5, 7, and 9 wt.% Fe/Ti ratios were dissolved together in 25 mL of demineralized water, then added dropwise into the Ti precursor with delicate stirring. The solution was further stirred over 30 min homogeneously and then separated by centrifugation at 1500 rpm for 1 h. The solid was aged in the open air for 48 h before being heated at 50 °C for 24 h. Finally, the material was calcined at 500 °C for 4 h under atmospheric conditions. Additionally, composite with 5 wt.% of Fe dopant was calcined at 700 and 900 °C. The composite materials are denoted as αFe-βN-ZT-γ, in which Fe, N, and ZT represent iron dopant, nitrogen dopant, and zirconium titanate composite, respectively. Moreover, α and β are the percentage of iron and nitrogen dopants, respectively, and γ is the calcination temperature in °C. All samples were characterized using XRD, FTIR, SRUV, and SEM-EDX.

■ RESULTS AND DISCUSSION

X-ray diffraction patterns of Fe-10N-ZT with various amounts of Fe after calcination at 500 °C are shown in Fig. 1. The reference materials were TiO_2, ZrO_2, ZT-500 (undoped $ZrTiO_4$), and 10N-ZT-500 (N-doped $ZrTiO_4$). The crystallite size of Fe-10N-ZT and references were calculated by using Debye-Scherrer equation [12] and presented in Table 2. The diffraction pattern of pure TiO_2 exhibits major peaks at 25° (d101) and 48° (d200), indicating TiO_2 in the anatase phase (ICDD: 00-021-1272). On the other hand, pure ZrO_2 reveals tetragonal phase appeared at 30° (d101), 50° (d112), and 60° (d211) (ICDD: 00-042-1164). Small peaks

Table 2. Crystallite size of ZrO_2, TiO_2, ZT-500, 10N-ZT-500 and various Fe-10N-ZT composites

Material	Crystal phase	hkl	2θ (°)	FWHM (°)	L (nm)
ZrO_2	Tetragonal	101	29.93	0.20	28.24
TiO_2	Anatase	101	25.11	0.32	17.65
ZT-500	Tetragonal	101	29.95	0.20	28.70
	Anatase	101	25.08	0.30	18.99
10N-ZT-500	Tetragonal	101	29.93	0.19	29.44
	Anatase	101	25.05	0.32	17.58
1Fe-10N-ZT-500	Tetragonal	101	29.99	0.20	28.88
	Anatase	101	25.11	0.44	12.86
3Fe-10N-ZT-500	Tetragonal	101	29.99	0.20	28.99
	Anatase	101	25.16	0.39	14.54
5Fe-10N-ZT-500	Tetragonal	101	30.06	0.20	28.08
	Anatase	101	25.26	0.38	14.78
7Fe-10N-ZT-500	Tetragonal	101	30.05	0.19	29.81
	Anatase	101	25.15	0.41	13.91

Table 2. Crystallite size of ZrO_2, TiO_2, ZT-500, 10N-ZT-500 and various Fe-10N-ZT composites (*Continued*)

Material	Crystal phase	hkl	2θ (°)	FWHM (°)	L (nm)
9Fe-10N-ZT-500	Tetragonal	101	30.04	0.20	28.27
	Anatase	101	25.00	0.29	19.56
5Fe-10N-ZT-700	Tetragonal	101	29.91	0.19	29.93
	Anatase	101	25.10	0.10	54.26
	Rutile	110	27.16	0.21	27.24
5Fe-10N-ZT-900	Tetragonal	101	30.03	0.19	30.67
	Rutile	110	27.30	0.18	31.56

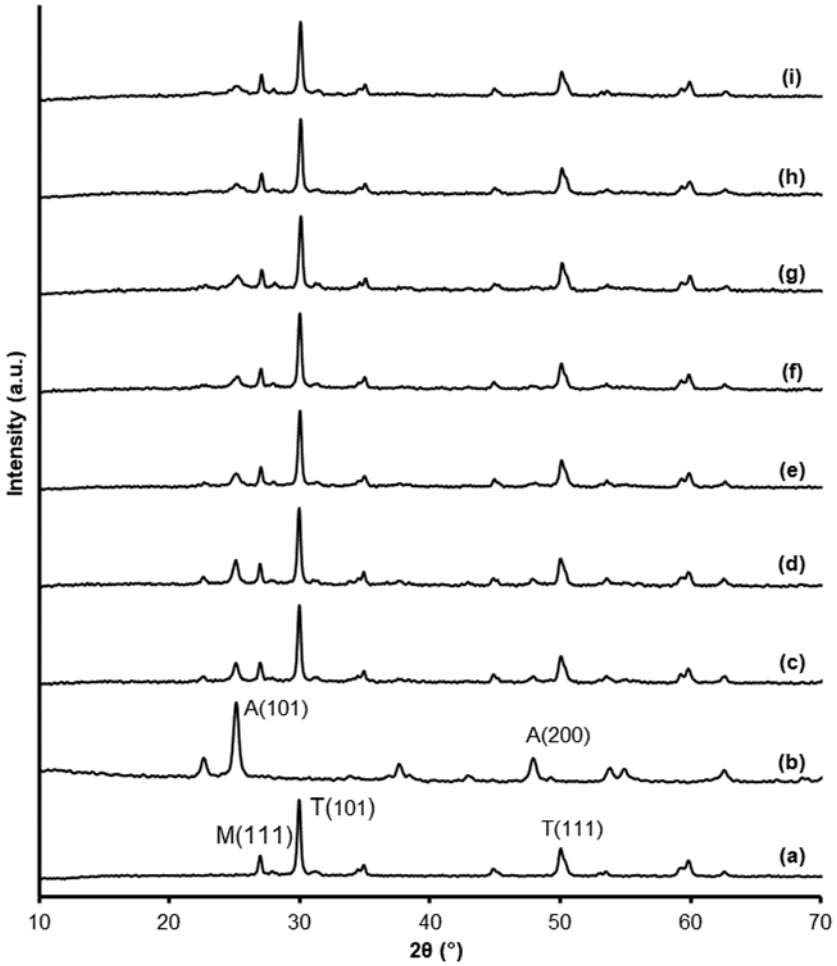

Fig 1. Diffraction patterns of (a) ZrO_2, (b) TiO_2, (c) ZT-500, (d) 10N-ZT-500, (e) 1Fe-, (f) 3Fe-, (g) 5Fe-, (h) 7Fe-, and (i) 9Fe-10N-ZT-500

around 27° (d111) and 51° (d220) correspond with the monoclinic phase (ICDD: 00-037-1484). The diffraction peak of 10N-ZT-500 at 25° (d101) shifts slightly to a lower angle than the ZT-500. This can be related to the insertion of a nitrogen atom into the crystal lattice, which has a higher ionic radius than the oxygen atom, destabilizing the crystalline structures [34]. The iron pattern was hardly observed in the XRD pattern, indicating the inclusion of Fe^{3+} replacing Ti^{4+} in the crystal lattice. This is confirmed by a shift to a higher angle in the anatase diffraction peak (101) in comparison to pure TiO_2 [35].

In comparison to pure TiO_2, the full width of half maximum (FWHM) at the diffraction peak corresponding to the anatase phase of TiO_2 (101) in the

ZT-500 sample was reduced. As a result, the crystal size increased from 17.65 nm to 18.99 nm, suggesting that ZrO_2 presence slightly enhances the formation of anatase from amorphous. Furthermore, the FWHM value of the diffraction peak corresponding to the anatase TiO_2 phase was slightly higher after N doping and increased significantly after the Fe and N codoping. These results indicate that codoping with Fe and N hinders TiO_2 crystal growth, resulting in smaller anatase crystals [36].

Fig. 2 presents the XRD patterns of 5Fe-10N-ZT calcined at various temperatures. After calcined at 700 °C, 5Fe-10N-ZT-700 displays typical rutile pattern (ICDD: 00-021-1276) at 27° (d110), 36° (d101), 41° (d111), and 54° (d211), whereas anatase pattern intensity at 25° (d101) and 48° (d200) diminish. The diffraction pattern of 5Fe-10N-ZT-900 shows an apparent rutile phase. Anatase peaks at 25° (d101) and 48° (d200) are still observable, but with considerably lower intensity. This confirms that the presence of ZrO_2, which is prominent as a supporting material, can impede the transition of anatase to rutile [25]. No rutile peaks were seen in 10N-ZT-500, indicating that doping with nitrogen does not promote the phase transition from anatase to rutile at 500 °C. As reported in the literature, using urea as a nitrogen precursor retards the transition from anatase to rutile [37].

Fig. 3 shows FT-IR spectra of various iron dopant contents in Fe-10N-ZT with ZrO_2, TiO_2, and 10N-ZT-500 as references. All the materials were calcined at 500 °C. A vibration around 3400 cm^{-1} appearing in all samples is recognized as O–H stretching vibration [38]. Vibration peaks at 512 cm^{-1} and 1635 cm^{-1} are related to Zr–O and Zr–OH vibrations, respectively, which confirms the presence of ZrO_2 [39]. Comparing 10N-ZT-500 with ZrO_2 and TiO_2, the peak intensity in the frequency of 1640 cm^{-1} becomes strong and sharp. This discrepancy confirms the existence of the N dopant in the crystal lattice [40]. In addition, this also shows that the concentration of the OH group is getting stronger, which can increase the photocatalytic ability because it acts as a hole trap and suppresses the electron-hole recombination process [41]. The broadband of all Fe-10N-ZT-500 in the range of 400–800 cm^{-1} can be attributed to the Ti–O and Fe–O stretching vibration [3]. A vibrational band was observed and increased around 1080 cm^{-1} as a percentage of iron arose, which might potentially be the vibration Fe–O–Zr or Fe–O–Ti, or both.

The FTIR spectra of 5Fe-10N-ZT following calcination at various temperatures are shown in Fig. 4. Higher calcination temperatures lower the intensity of O–H vibration at 3400 cm^{-1}. This is mainly due to the reduced water content caused by high-temperature

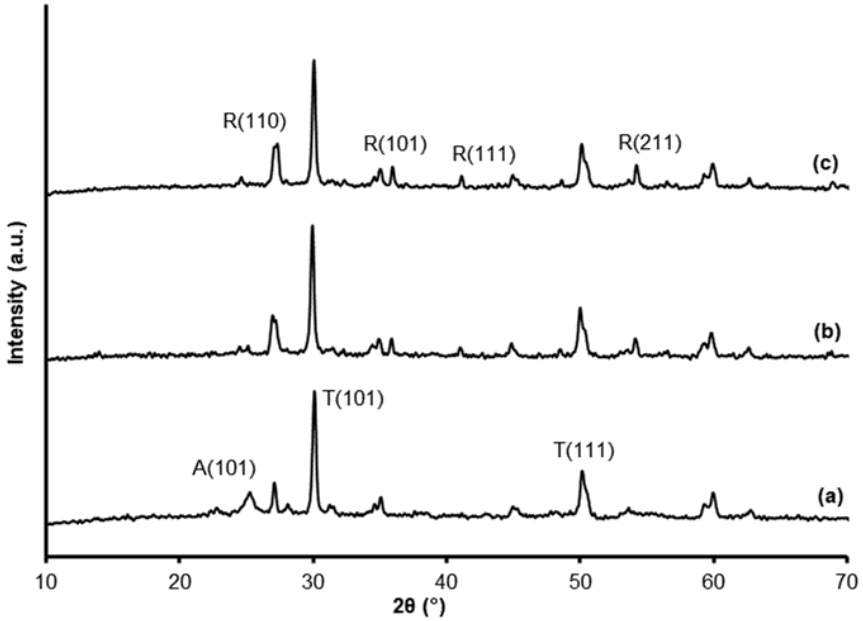

Fig 2. Diffraction patterns of 5Fe-10N-ZT (a) -500, (b) -700, and (c) -900

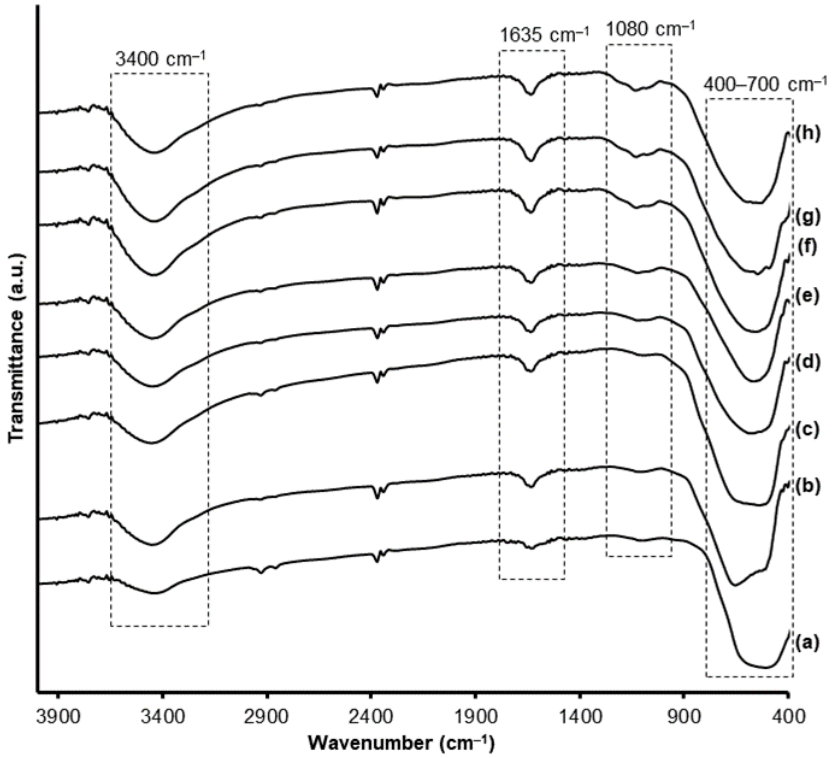

Fig 3. FT-IR spectra of (a) ZrO_2, (b) TiO_2, (c) 10N-ZT-500, (d) 1Fe-, (e) 3Fe-, (f) 5Fe-, (g) 7Fe-, and (h) 9Fe-10N-ZT-500

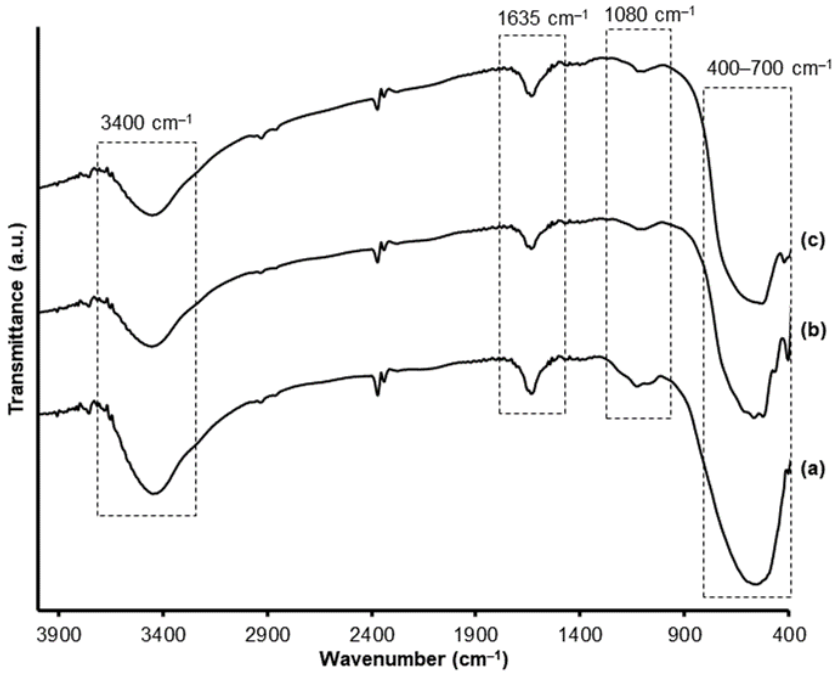

Fig 4. FTIR spectra of 5Fe-10N-ZT (a) -500, (b) -700, and (c) -900

calcination. The band of iron dopants at 1080 cm^{-1} decreases as the calcination temperature rises. This might be because the iron dopants are sintered at higher temperatures, lowering the Fe–O vibration. A sharp tip was noticed at 508 cm^{-1} after calcination at 700 and 900 °C, attributed to vibrations of the O–Ti–N or

N–Ti–N bonds. At a calcination temperature of 500 °C, the peak is less significant. Thus, it suggests that the Ti–N bond has not formed at 500 °C [42].

Table 3 lists the calculated bandgap (Eg) of various Fe-10N-ZT composites with TiO_2 as a reference. The bandgap was determined by analyzing the UV-Vis absorption spectra shown in Fig. 5. The regression method was used to obtain the turning point as the minimum absorbance, which will be calculated for the bandgap. All Fe-10N-ZT composites have Eg values below pure TiO_2 (3.12 eV). This proves that the presence of Fe and N dopants allows the absorption edge to shift to the visible light region (wavelength > 400 nm). It can be seen that the bandgap energy value of all Fe-10N-ZT samples is lower than that of 10N-ZT-500. The addition of 3 of wt.% Fe and 10 of wt.% N dopants is the optimal condition that gives the lowest bandgap value of 2.62 eV. The bandgap values increased as Fe content increased from 3 to 9 wt.% with a fixed amount of nitrogen. This might be owing to the agglomeration of iron that eliminates the doping effect. The result proves that codoping of $ZrTiO_4$ with Fe and N gives a significantly lower Eg value compared to the results of single transition metal doping in the previous work [30–33]. Possibly, this result occurred due to the contribution of Fe 3d and N 2p orbitals forming a new electron state above VB in the crystal lattice [43].

After calcined at 700 and 900 °C, the bandgap of 5Fe-10N-ZT showed a lower value. Based on the diffraction data, it can be seen that the TiO_2 phase transformation from anatase to rutile occurs at 700 °C. The rutile phase has a lower bandgap value than anatase, thus increasing the calcination temperature decreases the bandgap value. However, at 900 °C, the value of Eg is greater (2.81 eV) than at 700 °C (2.79 eV). This is probably because of the sintering effect, which leads to dopant agglomeration so that the dopant effect diminishes.

The morphology and particle size of the composites were identified through characterization by SEM-EDX. SEM images of ZrO_2 and 3Fe-10N-ZT-500 materials with a magnification of 15,000 times are shown in Fig. 6, along with their respective EDX spectra. Uniformly and spherical morphologies are seen in both the 3Fe-10N-ZT-500 and

Table 3. Bandgap data of various Fe-10N-ZT composites and TiO_2

Material	Eg (eV)
TiO_2	3.12
10N-ZT-500	2.78
1Fe-10N-ZT-500	2.67
3Fe-10N-ZT-500	2.62
5Fe-10N-ZT-500	2.82
5Fe-10N-ZT-700	2.79
5Fe-10N-ZT-900	2.81
7Fe-10N-ZT-500	2.88
9Fe-10N-ZT-500	2.91

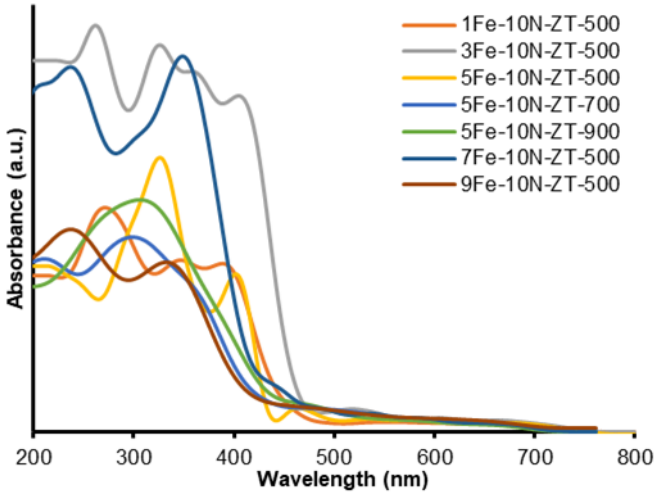

Fig 5. UV-Vis absorption spectra of various Fe-10N-ZT composites

and ZrO_2. There are agglomerations in some locations due to calcination. The 3Fe-10N-ZT-500 composite has a coarser surface than pure ZrO_2, while the particle size is similar with an estimated diameter of 0.2 μm.

The mass percentage of each element by EDX analysis is shown in Table 4. The results of the EDX spectra prove the presence of the main elements of the synthesized material. Ti is present on the surface of ZrO_2, indicated by the Zr-to-O ratio of 3Fe-10N-ZT-500 to be lower than that of ZrO_2. The 3Fe-10N-ZT-500 composite contained 1.5 and 2.8 wt.% of Fe and N dopants, respectively. Low quantities of dopants were used because a high amount of dopant may act as a recombination sites for photogenerated charges, decreasing the photocatalytic activity [44]. Despite the fact that the percentage is small, it does influence the

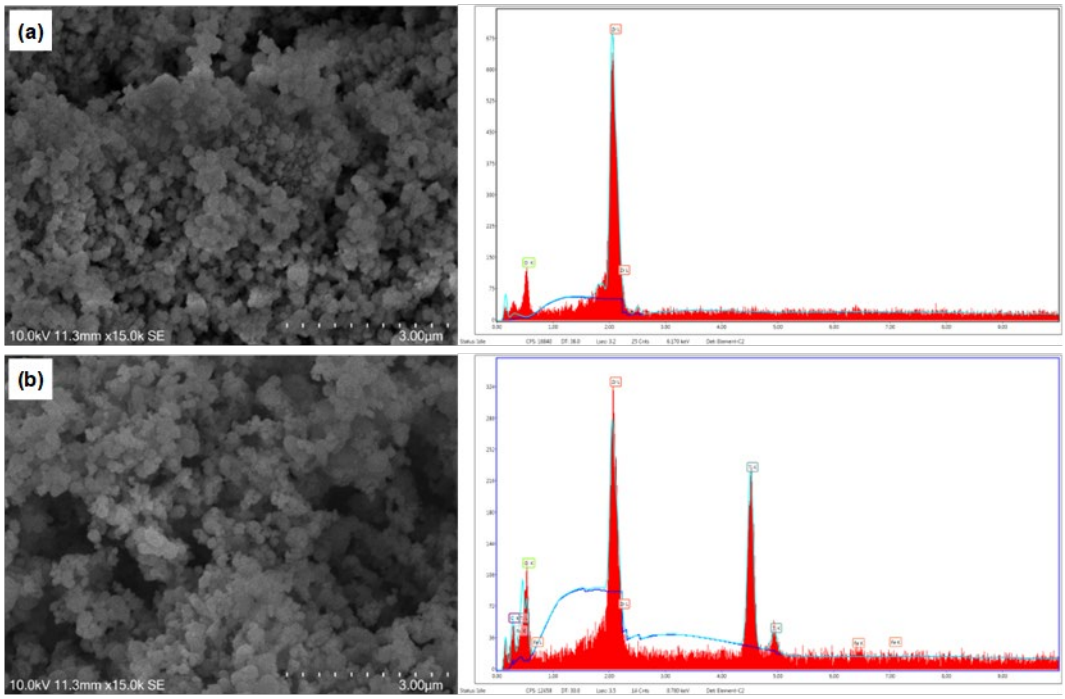

Fig 6. SEM images captured with 15,000× magnification and the corresponding EDX spectra of (a) ZrO_2 and (b) 3Fe-10N-ZT-500

Table 4. Elemental composition of ZrO_2 and 3Fe-10N-ZT-500 surfaces measured by X-ray energy dispersive spectroscopy

Material	% Mass						
	Zr	O	Ti	Fe	N	C	Total
ZrO_2	52.8	47.2	-	-	-	-	100
3Fe-10N-ZT-500	19.7	43.8	15.1	1.5	2.8	17.2	100

crystallite structure and light absorption of the material, as shown by XRD and SR-UV characterization.

■ CONCLUSION

The Fe,N-codoped $ZrTiO_4$ composites were successfully prepared through the sol-gel method. The incorporation of Fe and N dopants into $ZrTiO_4$ shifts the bandgap to the visible region and influences the crystal phase transformation. The composite with the lowest bandgap (2.62 eV) was obtained with 3 wt.% of Fe and 10 wt.% of N contents calcined at 500 °C. Furthermore, the XRD analysis proves that the presence of ZrO_2 prevents the anatase-to-rutile transformation at higher calcination temperatures than 500 °C. Fe,N-codoped $ZrTiO_4$ can be considered as a potentially active photocatalyst under visible light.

■ REFERENCES

[1] Huang, W.C., and Ting, J.M., 2017, Novel nitrogen-doped anatase TiO_2 mesoporous bead photocatalysts for enhanced visible light response, *Ceram. Int.*, 43 (13), 9992–9997.

[2] Zhang, J., Li, L., Xiao, Z., Liu, D., Wang, S., Zhang, J., Hao, Y., and Zhang, W., 2016, Hollow sphere TiO_2-ZrO_2 prepared by self-assembly with polystyrene colloidal template for both photocatalytic degradation and H_2 evolution from water splitting, *ACS Sustainable Chem. Eng.*, 4 (4), 2037–2046.

[3] Song, J., Wang, X., Bu, Y., Wang, X., Zhang, J., Huang, J., Ma, R.R., and Zhao, J., 2017, Photocatalytic enhancement of floating

photocatalyst: Layer-by-layer hybrid carbonized chitosan and Fe-N-codoped TiO_2 on fly ash cenospheres, *Appl. Surf. Sci.*, 391, 236–250.

[4] Kalantari, K., Kalbasi, M., Sohrabi, M., and Royaee, S.J., 2017, Enhancing the photocatalytic oxidation of dibenzothiophene using visible light responsive Fe and N co-doped TiO_2 nanoparticles, *Ceram. Int.*, 43 (1), 973–981.

[5] Zhang, J., Zhou, P., Liu, J., and Yu, J., 2014, New understanding of the difference of photocatalytic activity among anatase, rutile and brookite TiO_2, *Phys. Chem. Chem. Phys.*, 16 (38), 20382–20386.

[6] Lin, H.Y., and Shih, C.Y., 2015, Efficient one-pot microwave-assisted hydrothermal synthesis of M (M = Cr, Ni, Cu, Nb) and nitrogen co-doped TiO_2 for hydrogen production by photocatalytic water splitting, *J. Mol. Catal. A: Chem.*, 411, 128–137.

[7] Wang, J., Zhao, Y.F., Wang, T., Li, H., and Li, C., 2015, Photonic, and photocatalytic behavior of TiO_2 mediated by Fe, Co, Ni, N doping and co-doping, *Phys. B*, 478, 6–11.

[8] Zou, M., Feng, L., Ganeshraja, A.S., Xiong, F., and Yang, M., 2016, Defect induced nickel, nitrogen-codoped mesoporous TiO_2 microspheres with enhanced visible light photocatalytic activity, *Solid State Sci.*, 60, 1–10.

[9] Barkhade, T., and Banerjee, I., 2019, Optical properties of Fe doped TiO_2 nanocomposites synthesized by sol-gel technique, *Mater. Today: Proc.*, 18, 1204–1209.

[10] Zhang, Y., Shen, Y., Gu, F., Wu, M., Xie, Y., and Zhang, J., 2009, Influence of Fe ions in characteristics and optical properties of mesoporous titanium oxide thin films, *Appl. Surf. Sci.*, 256 (1), 85–89.

[11] Basavarajappa, P.S., Patil, S.B., Ganganagappa, N., Reddy, K.R., Raghu, A.V, and Reddy, C.V., 2020, Recent progress in metal-doped TiO_2, non-metal doped/codoped TiO_2 and TiO_2 nanostructured hybrids for enhanced photocatalysis, *Int. J. Hydrogen Energy*, 45 (13), 7764–7778.

[12] Cong, Y., Zhang, J., Chen, F., and Anpo, M., 2007, Synthesis and characterization of nitrogen-doped TiO_2 nanophotocatalyst with high visible light activity, *J. Phys. Chem. C*, 111 (19), 6976–6982.

[13] Shen, J.H., Tang, Y.H., Jiang, Z.W., Liao, D.Q., and Horng, J.J., 2021, Optimized preparation and characterization of Co-N codoped TiO_2 with enhanced visible light activity: An insight into effect of dopants on surface redox reactions of photogenerated charge carriers for hydroxyl radical formation, *J. Alloys Compd.*, 862, 158697.

[14] Linnik, O., Shestopal, N., Smirnova, N., Eremenko, A., Korduban, O., Kandyba, V., Kryshchuk, T., Socol, G., Stefan, N., Popescu-Pelin, G., Ristoscu, C., and Mihailescu, I.N., 2015, Correlation between electronic structure and photocatalytic properties of non-metal doped TiO_2/ZrO_2 thin films obtained by pulsed laser deposition method, *Vacuum*, 114, 166–171.

[15] Sinhmar, A., Setia, H., Kumar, V., Sobti, A., and Toor, A.P., 2020, Enhanced photocatalytic activity of nickel and nitrogen codoped TiO_2 under sunlight, *Environ. Technol. Innovation*, 18, 100658.

[16] Farkas, B., Budai, J., Kabalci, I., Heszler, P., and Geretovszky, Z., 2008, Optical characterization of PLD grown nitrogen-doped TiO_2 thin films, *Appl. Surf. Sci.*, 254 (11), 3484–3488.

[17] Di Valentin, C., Pacchioni, G., and Selloni, A., 2004, Origin of the different photoactivity of N-doped anatase and rutile TiO_2, *Phys. Rev. B: Condens. Matter Mater. Phys.*, 70 (8), 085116.

[18] Gurushantha, K., Anantharaju, K.S., Nagabhushana, H., Sharma, S.C., Vidya, Y.S., Shivakumara, C., Nagaswarupa, H.P., Prashantha, S.C., and Anilkumar, M.R., 2015, Facile green fabrication of iron-doped cubic ZrO_2 nanoparticles by *Phyllanthus acidus*: Structural, photocatalytic and photoluminescent properties, *J. Mol. Catal. A: Chem.*, 397, 36–47.

[19] de Moraes, N.P., de Azeredo, C.A.S.H., Bacetto, L.A., da Silva, M.L.C.P., and Rodrigues, L.A., 2018, The effect of C-doping on the properties and photocatalytic activity of ZrO_2 prepared via sol-gel route, *Optik*, 165, 302–309.

[20] Syoufian, A., Manako, Y., and Nakashima, K., 2015, Sol-gel preparation of photoactive srilankite-type zirconium titanate hollow spheres by templating sulfonated polystyrene latex particles, *Powder Technol.*, 280, 207–210.

[21] Kim, J.Y., Kim, C.S., Chang, H.K., and Kim, T.O., 2010, Effects of ZrO_2 addition on phase stability and photocatalytic activity of ZrO_2/TiO_2 nanoparticles, *Adv. Powder Technol.*, 21 (2), 141–144.

[22] Chang, S.M., and Doong, R.A., 2006, Characterization of Zr-doped TiO_2 nanocrystals prepared by a nonhydrolytic sol-gel method at high temperatures, *J. Phys. Chem. B*, 110 (42), 20808–20814.

[23] Wan, L., Gao, Y., Xia, X.H., Deng, Q.R., and Shao, G., 2011, Phase selection and visible light photo-catalytic activity of Fe-doped TiO_2 prepared by the hydrothermal method, *Mater. Res. Bull.*, 46 (3), 442–446.

[24] Kumar, K.D., Kumar, G.P., and Reddy, K.S., 2015, Rapid microwave synthesis of reduced graphene oxide-supported TiO_2 nanostructures as high performance photocatalyst, *Mater. Today: Proc.*, 2 (4-5), 3736–3742.

[25] Abdelhaleem, A., Chu, W., and Liang, X., 2019, Diphenamid degradation via sulfite activation under visible LED using Fe (III) impregnated N-doped TiO_2 photocatalyst, *Appl. Catal., B*, 244, 823–835.

[26] Saidani, T., Zaabat, M., Aida, M.S., Benaboud, A., Benzitouni, S., and Boudine, A., 2014, Influence of annealing temperature on the structural, morphological and optical properties of Cu doped ZnO thin films deposited by the sol-gel method, *Superlattices Microstruct.*, 75, 47–53.

[27] Sharon, M., Modi, F., and Sharon, M., 2016, Titania based nanocomposites as a photocatalyst: A review, *AIMS Mater. Sci.*, 3 (3), 1236–1254.

[28] Aba-Guevara, C.G., Medina-Ramírez, I.E., Hernández-Ramírez, A., Jáuregui-Rincón, J., Lozano-Álvarez, J.A., and Rodríguez-López, J.L., 2017, Comparison of two synthesis methods on the preparation of Fe, N-Co-doped TiO_2 materials for degradation of pharmaceutical compounds under visible light, *Ceram. Int.*, 43 (6), 5068–5079.

[29] Ning, Q., Zhang, L., Liu, C., Li, X., Xu, C., and Hou, X., 2021, Boosting photogenerated carriers for organic pollutant degradation via in-situ constructing atom-to-atom $TiO_2/ZrTiO_4$ heterointerface, *Ceram. Int.*, 47 (23), 33298–33308.

[30] Kurniawan, R., Sudiono, S., Trisunaryanti, W., and Syoufian, A., 2019, Synthesis of iron-doped zirconium titanate as a potential visible-light responsive photocatalyst, *Indones. J. Chem.*, 19 (2), 454–460.

[31] Andita, K.R., Kurniawan, R., and Syoufian, A., 2019, Synthesis and characterization of Cu-doped zirconium titanate as a potential visible-light responsive photocatalyst, *Indones. J. Chem.*, 19 (3), 761–766.

[32] Alifi, A., Kurniawan, R., and Syoufian, A., 2020, Zinc-doped titania embedded on the surface of zirconia: A potential visible-responsive photocatalyst material, *Indones. J. Chem.*, 20 (6), 1374–1381.

[33] Sulaikhah, E.F., Kurniawan, R., Pradipta, M.F., Trisunaryanti, W., and Syoufian, A., 2020, Cobalt doping on zirconium titanate as a potential photocatalyst with visible-light-response, *Indones. J. Chem.*, 20 (4), 911–918.

[34] Lee, H.U., Lee, S.C., Choi, S., Son, B., Lee, S.M., Kim, H.J., and Lee, J., 2013, Efficient visible-light induced photocatalysis on nanoporous nitrogen-doped titanium dioxide catalysts, *Chem. Eng. J.*, 228, 756–764.

[35] Wang, Q., Jin, R., Zhang, M., and Gao, S., 2017, Solvothermal preparation of Fe-doped TiO_2 nanotube arrays for enhancement in visible light induced photoelectrochemical performance, *J. Alloys Compd.*, 690, 139–144.

[36] Suwannaruang, T., Hildebrand, J.P., Taffa, D.H., Wark, M., Kamonsuangkasem, K., Chirawatkul, P., and Wantala, K., 2020, Visible light-induced degradation of antibiotic ciprofloxacin over Fe–N–TiO_2 mesoporous photocatalyst with

anatase/rutile/brookite nanocrystal mixture, *J. Photochem. Photobiol., A*, 391, 112371.

[37] Suwannaruang, T., Kidkhunthod, P., Chanlek, N., Soontaranon, S., and Wantala, K., 2019, High anatase purity of nitrogen-doped TiO_2 nanorice particles for the photocatalytic treatment activity of pharmaceutical wastewater, *Appl. Surf. Sci.*, 478, 1–14.

[38] Realpe Jimenez, A., Nuñez, D., Rojas, N., Ramirez, Y., and Acevedo, M., 2021, Effect of Fe–N codoping on the optical properties of TiO_2 for use in photoelectrolysis of water, *ACS Omega*, 6 (7), 4932–4938.

[39] Arafati, A., Borhani, E., Nourbakhsh, S.M.S., and Abdoos, H., 2019, Synthesis and characterization of tetragonal/monoclinic mixed phases nanozirconia powders, *Ceram. Int.*, 45 (10), 12975–12982.

[40] Di, K., Zhu, Y., Yang, X., and Li, C., 2006, Electrorheological behavior of urea-doped mesoporous TiO_2 suspensions, *Colloids Surf., A*, 280 (1-3), 71–75.

[41] Neppolian, B., Wang, Q., Yamashita, H., and Choi, H., 2007, Synthesis and characterization of ZrO_2-TiO_2 binary oxide semiconductor nanoparticles: Application and interparticle electron transfer process, *Appl. Catal., A*, 333 (2), 264–271.

[42] Nolan, N.T., Synnott, D.W., Seery, M.K., Hinder, S.J., Van Wassenhoven, A., and Pillai, S.C., 2012, Effect of N-doping on the photocatalytic activity of sol–gel TiO_2, *J. Hazard. Mater.*, 211-212, 88–94.

[43] Li, Z., Wang, X., Jia, L., and Chi, B., 2014, Synergistic effect in Fe/N co-doped anatase TiO_2 (101) surface and the adsorption of di-, tri- and polyatomic gases: A DFT investigation, *J. Mol. Struct.*, 1061, 160–165.

[44] Jaiswal, R., Bharambe, J., Patel, N., Dashora, A., Kothari, D.C., and Miotello, A., 2015, Copper and nitrogen co-doped TiO_2 photocatalyst with enhanced optical absorption and catalytic activity, *Appl. Catal., B*, 168-169, 333–341.